

Short-Period Variables in TESS Full-Frame Image Light Curves Identified via Convolutional Neural Networks

GREG OLMSCHENK,^{1,2} RICHARD K. BARRY,¹ STELA ISHITANI SILVA,^{1,3} BRIAN P. POWELL,¹ ETHAN KRUSE,¹
JEREMY D. SCHNITTMAN,¹ AGNIESZKA M. CIEPLAK,⁴ THOMAS BARCLAY,¹ SIDDHANT SOLANKI,¹ BIANCA ORTEGA,¹
JOHN BAKER,¹ AND YESENIA HELEM SALINAS MAMANI⁵

¹NASA Goddard Space Flight Center, Greenbelt, MD 20771, USA

²Department of Astronomy, University of Maryland, College Park, MD 20742, USA

³Department of Physics, The Catholic University of America, Washington, DC 20064, USA

⁴Space Sciences Laboratory, 7 Gauss Way, University of California, Berkeley, CA 94720-7450, USA

⁵Computer Science Department, School of Engineering, Pontificia Universidad Católica de Chile, Chile

(Received 2023-12-29)

Submitted to The Astronomical Journal

ABSTRACT

The *Transiting Exoplanet Survey Satellite* (*TESS*) mission measured light from stars in ~85% of the sky throughout its two-year primary mission, resulting in millions of *TESS* 30-minute cadence light curves to analyze in the search for transiting exoplanets. To search this vast dataset, we aim to provide an approach that is both computationally efficient, produces highly performant predictions, and minimizes the required human search effort. We present a convolutional neural network that we train to identify short period variables. To make a prediction for a given light curve, our network requires no prior target parameters identified using other methods. Our network performs inference on a *TESS* 30-minute cadence light curve in ~5ms on a single GPU, enabling large scale archival searches. We present a collection of 14156 short-period variables identified by our network. The majority of our identified variables fall into two prominent populations, one of short-period main sequence binaries and another of Delta Scuti stars. Our neural network model and related code is additionally provided as open-source code for public use and extension.

1. INTRODUCTION

The volume of astronomical photometric datasets is expanding rapidly. Due to their size, these datasets often contain data that no human eye has ever nor will ever see. Because of this, automated systems that can filter irrelevant information and identify interesting phenomena is imperative. In this work, we describe our development and application of a neural network (NN) to automatically identify short-period variables in the *Transiting Exoplanet Survey Satellite* (*TESS*, Ricker et al. 2014) full-frame image (FFI) data.

Short-duration periodic variability offers physical insight into some of the most extreme conditions for stars and stellar remnants. Modern wide-field surveys such as *TESS*, the Optical Gravitational Lensing Experiment (Soszyński et al. 2015) and the Zwicky Transient Facility (Graham et al. 2019) offer the possibility of developing and testing population synthesis models that provide insights into the distribution of variables in the

Galaxy and they can help describe stellar evolutionary processes.

The primary goal of the *TESS* mission, the observatory whose data was used for work, is to detect the signature of planets as they transit in front of their host stars. Launched in April 2018, *TESS* is performing a near all-sky photometric survey intended to identify planets with bright enough host stars to enable mass estimation from ground-based radial velocity measurements. Importantly, due to *TESS*'s high observational cadence, these data are also well-suited to search for various other forms of short-duration, time-domain astrophysical phenomena.

The *TESS* observatory is positioned in a high-Earth elliptical orbit of 13.7 days. *TESS* completed its 2-year primary mission in July 2020. While a principle data product of *TESS*'s primary mission is the 2-minute cadence photometry of more than 200,000 stars, of more relevance for this work is the FFI data. At a 30-minute cadence, *TESS* took flux measurements of its entire field of view (24° × 96°). This FFI data includes approximately

85% of the sky and observes of billions of sources (Ricker et al. 2014). Searching this large-scale dataset requires a robust and computationally fast method and NNs provide one such approach.

Largely due to their potential to approximate any given function (Cybenko 1989; Leshno et al. 1993; Zhou 2020), in recent years, deep neural networks (DNNs, e.g., LeCun et al. 2015) have come to dominate the field of machine learning (ML). In the case of photometric data, a common function these methods may be tasked to learn is to convert observed flux measurements into physical classifications of the sources. Both ML and non-ML algorithms can only approximate the unknown ideal function that can perform this conversion perfectly.

When a NN is trained to learn this function, it attempts to learn optimal data transformations (Rumelhart et al. 1986), which can potentially lead to more accurate classifications than manually designed methods, often because these methods frequently omit data during processing. For instance, often outlier data points are filtered prior to period estimation. However, such filtering can often remove potentially useful information. In contrast to this, NNs do not directly remove sources of noise. Instead, they learn to identify such noise, while retaining signal within it, and incorporate this information into their predictions about the likelihood of a light curve (LC) containing the desired signal, in this case, a short-period signal. This approach makes them effective at processing noisy data (Dong et al. 2014; Hinton et al. 2012; Xu et al. 2014). For instance, if outliers occur due to a temporary systematic offset within the LC, as is common in *TESS* data, but still carry the periodic signal, the relevant information for detecting the periodic signal can be retained by the NN where a simple omission of outliers would remove it.

As a generalized function approximator (Cybenko 1989; Leshno et al. 1993; Zhou 2020), a sufficiently large NN is capable of learning any hand-crafted function arbitrarily well, such as a function to produce a periodogram for a LC. Furthermore, if improvements can be made to the hand-crafted transformation that yields improved results, a NN has the capability to learn that improved function instead. This inherent property of NNs gives them the potential to outperform their hand-crafted counterparts.

The computational speed of the method is another advantage of using NNs in detecting short-period signals. Our NN can infer on a FFI LC in ~ 5 ms using a single GPU, enabling us to perform an inference on our entire dataset of ~ 67 million LCs in a few days on a single GPU.

1.1. Short-period main sequence binaries background

The first of the two large populations identified by our NN are short-period main sequence (MS) binaries, which, at the shortest periods, consist of red dwarf stars. Although red dwarf stars are extremely common, how they evolve in close binary systems, including in contact binaries, is not well understood. There is a dramatic cut-off of such binaries at ~ 0.22 days Rucinski (1992, 2007). Notably, the reason for this cut-off is still under investigation. The cut-off was originally often attributed to the stars reaching their fully convective limit (Rucinski 1992). More recently, magnetic braking (Stepien 2007) and unstable mass transfer (Jiang et al. 2012) have been implicated of playing a prominent role. At any rate, a larger sample size may help to more clearly define the evolutionary and formation processes of these and other short-period MS binaries.

1.2. Delta Scuti background

Delta Scuti (δ Sct) stars constitute a distinct type of pulsating variable star with intermediate mass, 1.5–2.5 solar masses (Bedding et al. 2020), located at the intersection of the classical instability strip (Dupret et al. 2004) and the MS stars on the Hertzsprung-Russell (HR) diagram (Handler 2009; Breger 2000). Typically of spectral types A to F, δ Sct stars class is composed of both Pop I and Pop II stars¹. These stars, characterized by a period range spanning from 0.02 days to 0.25 days, demonstrate multiperiodic luminosity variability and can present both radial and non-radial pulsations (Breger 2000).

Stellar pulsations serve as a valuable tool in investigating the internal structures of stars. The excitation mechanism underlying these pulsations involves the cyclic transfer of kinetic energy from the internal energy of the mixture of gas and radiation in the ionization zones, particularly rich in elements like Helium and Hydrogen. By identifying the natural frequencies of their pulsation modes, it is possible to compare these observations with theoretical models improving our understanding of stellar properties and their evolutionary processes (Breger 2000; Bedding et al. 2020). Notably, δ Sct stars were among the first pulsators whose asteroseismic potential was recognized (Handler 2009).

As stars evolve, they may cross the instability strip and may pulsate. They could be stars moving from the MS to the giant branch or pre-MS stars evolving to zero-age main sequence (ZAMS) (Breger 2000, 1972). δ Sct stars have also been detected in diverse scenarios, ranging from eclipsing binaries (Kahraman Aliçavuş et al. 2023)

¹ Baade (1944)

to stars populating other galaxies (Mateo et al. 1998). This broad range of detection highlights that δ Sct stars are not uncommon.

2. DATA

In this work, we have used LC data, *i.e.*, measures of flux over time. Figure 1 shows an example of a *TESS* LC, showing flux vs. time of the *TESS* target for TIC ID 149989733 sector 10. The time is given in *TESS* Barycentric Julian Day (BTJD) time (Tenenbaum & Jenkins 2018). With the Julian Day in the Barycentric Dynamical Time standard (BJD), $\text{BTJD} = \text{BJD} - 2457000.0$. BJD is used for its accurate time standard which accounts for many different timing corrections, including leap seconds (*e.g.*, Eastman et al. 2010). The flux given is median normalized flux for the LC. The LCs were produced by the *eleanor* pipeline (Feinstein et al. 2019) from raw flux measurements provided by *TESS*.

The LC shown in Figure 1 is a typical example of a short-period variable identified by our NN. There is a gap in the middle of the data caused by the spacecraft pausing its observing to downlink data to Earth (Tenenbaum & Jenkins 2018). Notably, since the variables we are searching for range from 1 hour to 5 hours, the FFI cadence of 30 minutes results in very few data points per period. The LC shown in Figure 1 has a period of 1.326 hours, resulting in only 2 or 3 data points per period. This makes it difficult for a human to identify the periodicity in the unfolded LCs. Figure 1 shows an example from our δ Sct clusters (see Section 4.1 for clusters explanation). Figure 2 shows another example LC, this time taken from our MS binary cluster.

Ideally, a LC would contain only the flux from a single *TESS* target (typically a star system). However, in reality each *TESS* pixel covers ~ 21 arcseconds of the sky, and *TESS*'s point spread function results in blending between pixel measurements. For these reasons, a LC will contain flux from multiple targets. This often makes it challenging to determine which source the signal (or noise) is originating from.

TESS takes measurements of a large portion of the sky at regular intervals. During the primary mission, this interval was every 2 minutes. However, due to limitations of the spacecraft's storage and downlinking capabilities, only a small portion of this 2-minute cadence data is stored and downlinked (Ricker et al. 2014). However, at a 30-minute cadence all pixels' accumulated values are downlinked to Earth. These FFIs cover a much larger number of targets at a lower time resolution (Tenenbaum & Jenkins 2018). We used ~ 67 million 30-minute cadence LCs (with *TESS* magnitudes < 15) in this work, and this is the primary data set investigated by our NN.

2.1. Full-frame image light curve production

For details of the FFI LC production, see Powell et al. (2022). Briefly, Powell et al. (2022) used the 129,000-core *Discover* supercomputer at the NASA Center for Climate Simulation, to build FFI LCs for all sources observed by *TESS* down to 15th magnitude. All original and calibrated FFIs were produced by the *TESS* Science Processing Operations Center (Jenkins et al. 2016). Target lists were created through a parallelized implementation of *tess-point* (Burke et al. 2020) on the *TESS* input catalog (TIC, Stassun et al. 2018) provided by the Mikulski Archive for Space Telescopes (2020). The LCs for each sector were constructed in 1–4 days of wall clock time (for a total of over 100 CPU-years), depending on the density of targets in the sector, through a parallelized implementation of the *eleanor* Python module (Feinstein et al. 2019). ~ 67 million LCs were used for this work. As of this writing, the LCs of the first 9 sectors of the *TESS* primary mission data have been made publically available by Powell et al. (2022). We have used the full 26 sectors of the primary mission in this work. The public data release of the remaining primary mission sectors of the data by Powell et al. (2022) is still ongoing. These single sector LCs are the input to the pre-processing and, subsequently, our NN.

3. NEURAL NETWORK PIPELINE

The NN architecture and data preprocessing used in this work is the same as in Olmschenk et al. (2021). In that work, we developed a NN to identify transiting planets in *TESS* FFI data. The NN architecture and data preprocessing from Olmschenk et al. (2021) were designed with the intent to be generalizable and many of the explanations of design choices given there directly translate to the use case of short-period variables as well. Where we feel the connection is not immediately intuitive, we include additional explanation below. Also provided in Olmschenk et al. (2021) is a short primer to NNs which we believe will be helpful for readers of this work who are not familiar with NNs.

3.1. Training data

When designing and training the network, we use 80% of the available TIC IDs as the training data targets and use another 10% as validation data targets. These are data that are set aside that the network is not trained on. Instead, these data are used to evaluate the predictive performance of the network during the training process. This entails measuring the correctness of the network predictions on the validation data, which the network has not been trained with but where we know the correct answer. The remaining 10% is reserved to be used as

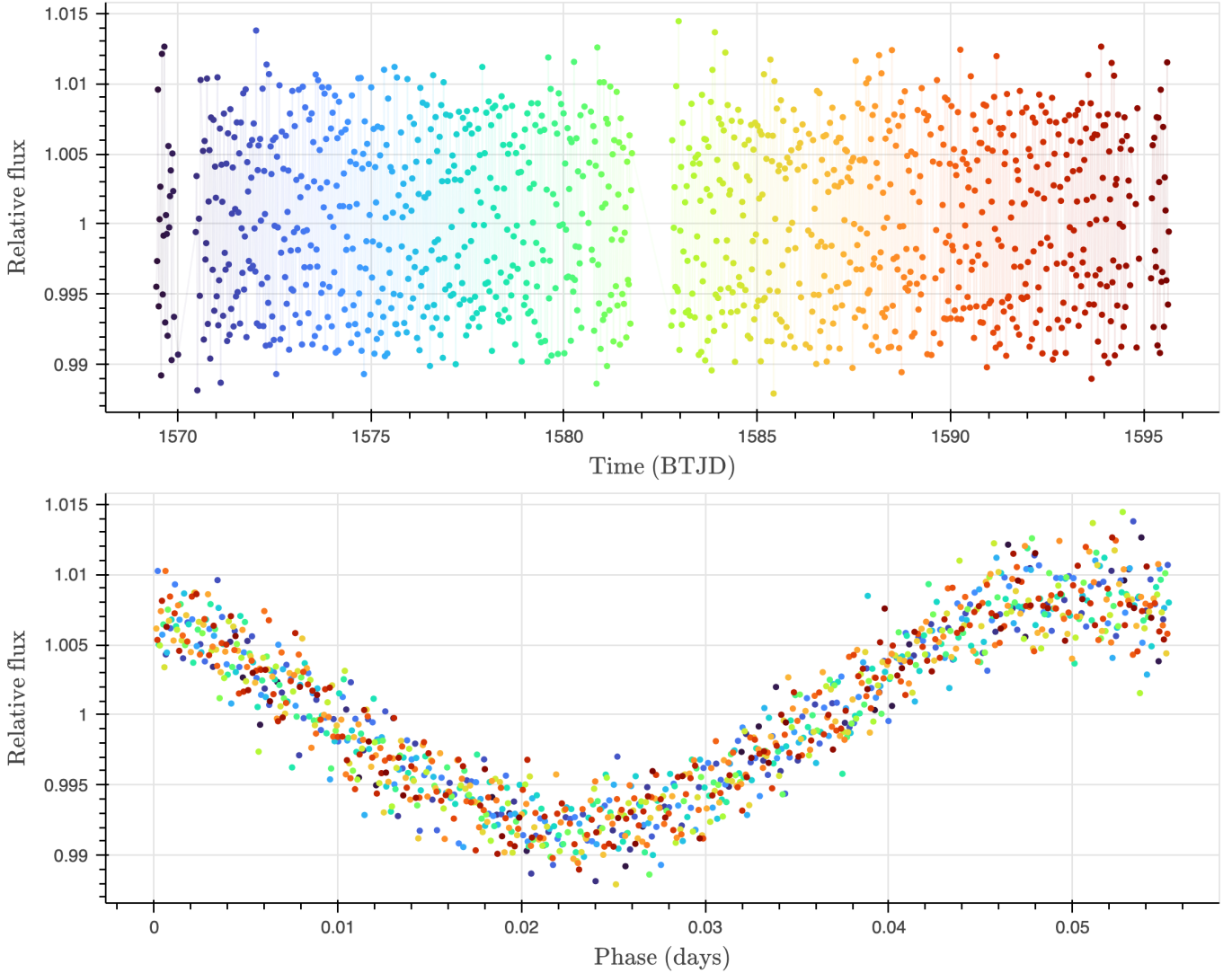


Figure 1. The FFI light curve and folded light curve for TIC ID 149989733 sector 10. This light curve was chosen as a typical example of the light curves identified by our NN. A notable aspect is that only 2 or 3 data points exist for each period (1.326 hours), resulting in the periodicity not being clear to a human observer in the unfolded light curve. Despite no specific periodicity-detecting mechanisms being included in the NN, it learns to identify such periods in the unfolded data. Color is based on unfolded time. This is an example from our δ Sct clusters.

a test dataset for a future evaluation. The test data is intended to evaluate the trained network after all design decisions are finalized. Several of the specific network and training configuration decisions were guided by preliminary performance results on the validation data. However, this validation data evaluation and the test data evaluation are beyond the scope of this work. The synthetic data used for training was not designed to accurately reflect the true distribution of expected periodic signals. Instead, it was designed to be a dataset which would produce a trained NN that can identify short-period targets.

Our training data consists of three collections of LCs. First, are the regular *TESS* LCs. These are treated as

negative samples during training. Although there will be rare false negative samples in this collection, due to their rarity and the NN’s statistical nature, they have minimal impact on the training process. The second collection is the same real *TESS* LCs, but injected with synthetic short periodic signals. The synthetic periodic signals are mixed sine and sawtooth signals. Due to the relatively small number of data points per period and the many variations of signals that can be produced with such a mixed signal, we found these synthetic signals to be sufficient to train our NN. These are the positive examples used during training. The third collection is the same real *TESS* LCs injected with synthetic long-period signals. We use this collection as a hard negative

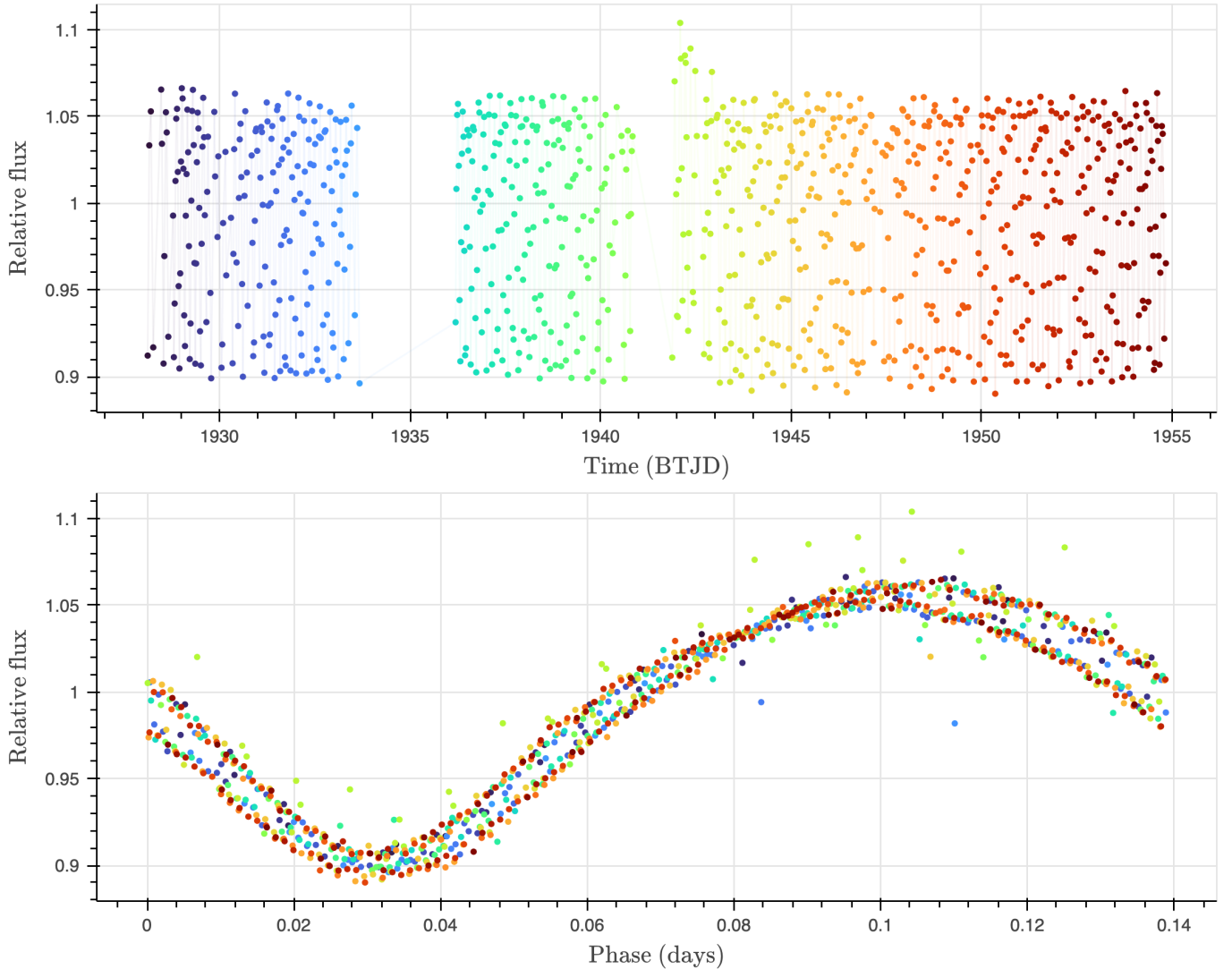


Figure 2. The FFI light curve and folded light curve for TIC ID 159971257 sector 23. An example from our MS binary cluster with clearly distinct binary signal peaks. Presented the same as Figure 1. See Figure 1 for details.

training case as it prevents the NN from fitting some artifact of the data (e.g., looking for a perfect sawtooth wave existing in the signal) and instead requires the network focus on the feature we are interested in (e.g., short periodicity).

The following are the specifics of the synthetic signals we generated. A period is selected from $\mathcal{U}(0.25, 5)$ hours for the short-period signals and from $\mathcal{U}(9, 20)$ hours for the long-period signals. Each signal had an amplitude selected from $\mathcal{U}(0.001, 1)$ independently for both the sine and sawtooth component. A random phase from $\mathcal{U}(0, \tau)$ was selected to offset the sine and sawtooth components. The fraction of the sawtooth cycle which consisted of the rising ramp was selected from $\mathcal{U}(0, 1)$ (with the remainder being the falling ramp). During the training process, for each training sample, a new random signal was generated

on-the-fly. The signal was injected at a random phase into the real *TESS* LC.

3.2. Network architecture

In this work, we use a 1D convolutional neural network (CNN, Krizhevsky et al. 2012) that was originally designed and developed in Olmschenk et al. (2021). This NN architecture is shown in Figure 3. Refer to Olmschenk et al. (2021) for the details of the CNN design.

Our NN framework code is available at <https://github.com/golmschenk/ramjet> (see https://github.com/golmschenk/ramjet/releases/tag/short_period_variable_neural_network_paper for the code version used in this work). This framework is also installable as a PyPI package (<https://pypi.org/project/astroramjet/>). Documentation for the NN framework can be found at <https://astroramjet.readthedocs.io/en/latest/>. This

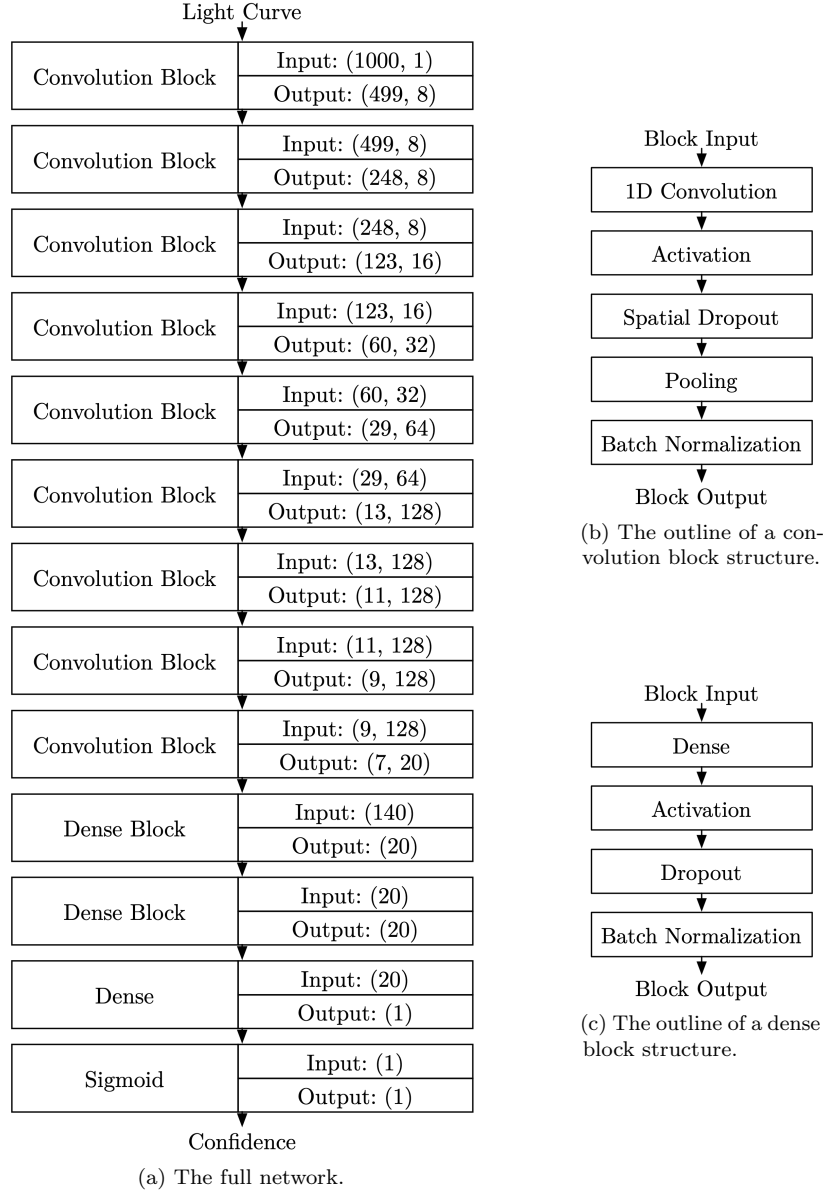


Figure 3. An overview of the architecture of the convolutional neural network used in this work. See Olmschenk et al. (2021) for details. All convolution/dense layers within a block use a number of filters/units equivalent to the size of the last dimension of their output tensor. A kernel size of 3 is used in all convolutional layers. For clarity of the diagram, three deviations from the diagram blocks are not shown. First, the first convolution block and the last dense block do not apply dropout or batch normalization. Second, the final convolution block uses a standard dropout instead of spatial dropout as the following layer is a dense layer. Third, pooling is only used by the first 6 convolution blocks. The remaining convolution blocks do not use pooling.

NN framework is a generalized photometric NN framework. Our code that applies this generalized framework to the specific task of short-period variable identification can be found at <https://github.com/golmschenk/generalized-photometric-neural-network-experiments>.

Similar to the situation in Olmschenk et al. (2021), the 1D CNN is an apt choice for searching for short-period variables due to how it constructs high-level global features from low-level local features. First, we expect the NN to find features such as individual peaks and

troughs as low-level features. In early layers, the NN will likely ignore the positions of these features in the LC, and only determine their presence based on the local LC shape. As such, the early layers of our network are convolutional layers, which treat each segment of the LC identically (Krizhevsky et al. 2012), *e.g.*, they search each portion of the LC for a peak or trough occurring in that location. Only after local level features, *e.g.*, individual wave cycles, are discovered do we expect the network to combine these features into global level

features—in this case repeating periodic wave cycles. The other advantages of a CNN, such as its prevention of overfitting, are the same as explained in [Olmschenk et al. \(2021\)](#).

No prior short-period variable parameter information is required by our NN; the only inputs to the NN are the fluxes of the LCs. Inference on a LC is performed by the NN in ~ 5 ms on a single GPU. This allows for inference of the entire ~ 67 M LCs FFI dataset to be completed in a few days.

The specific number of layers and size of each layer (as seen in [Figure 3](#)) was decided through limited experimentation. While a systematic search of network structures is beyond the scope of this work, we note that a minor change to our NN (*e.g.*, adding/removing a layer), while adjusting the remainder of the NN to produce the same output size, does not produce a trained NN that produces extremely different results.

3.3. Pre-processing

We use the same pre-processing of the LCs as in [Olmschenk et al. \(2021\)](#). This the primary purpose of this pre-processing is to prevent network overfitting and to encourage generalization of learned features. Briefly, during the training phase, a random data point removal is applied and a random rolling of the data is applied. During both the training phase and the inference phase, a uniform lengthening is applied and a modified z-score normalization is applied. See [Olmschenk et al. \(2021\)](#) for details on these pre-processing methods and why they are applied.

3.4. Post-neural network processing

After the neural network has identified likely short-period variable candidates, we run a process on candidates to determine the periodicity and remove false positives. The complete code used to perform this processing can be found at <https://github.com/golmschenk/generalized-photometric-neural-network-experiments>. Below we describe the most salient points.

First, we selected the top 50,000 LCs given the highest confidence score from the NN.

Then, we estimated candidate periodicity using a Lomb-Scargle periodogram. The Lomb-Scargle periodogram search was limited to a period of 1 hour (twice the sampling rate of *TESS* FFIs) up to 10 days. From the resulting periodogram, of the frequencies with a power within 10% of the max power, we take the highest frequency, then find the local power maximum from that frequency. We take this frequency/period as the variable frequency/period. Any targets with periods greater than 5 hours are discarded. These steps are chosen to reduce

the chances of choosing a shorter period alias. Here, we also fold the light curve, and binning into 25 bins in phase space, determine the minimum and maximum bins of the light curve based on the median value of the bin.

Next, we remove false positives which have photometric centers of variability that do not align with the target. This is done to prevent cases where a nearby variable is the real source of the variability. To accomplish this, we first use *TESScut* ([Brasseur et al. 2019](#)) to obtain the time-series raw image data of the pixels surrounding the target. We use an image of 10×10 centered on the target. The time-series image data is folded on the period determined previously, and again placed into 25 bins across phase space determined previously. Those which fall into the minimum and maximum bins of the previous step are used for the following variability photometric centroid estimation. We find median values of the binned images for the minimum and maximum bins, then take the difference of these resulting values. The centroid of these values is compared to estimated position of target from the TIC. If the estimated centroid is separated from the target position by more than 21 arcseconds (the angular size of a side of a *TESS* pixel), the candidate is discarded.

The amplitude is estimated as half of the difference between the maximum and minimum of the above binning. The relative amplitude is this previous amplitude divided by the median flux. The version of the relative amplitude with contamination uses the median flux of the original light curve. The version of the relative amplitude without contamination scales this value to take into account the estimated contamination ratio provided via the TIC where available.

Additional target stellar properties are taken from the TIC and the Gaia Mission ([Gaia, Brown et al. 2018](#)) where available.

4. RESULTS

The table of our identified short-period variable candidates is available as a supplemental file to this work. [Table 1](#) shows a random² sample of 100 rows from the complete table.

[Figure 4](#) shows the distribution of the periods of the candidates. These periods are compared against the effective temperatures of the variables in [Figure 5](#). The longer period cluster to correspond to MS binaries while

² To prevent the presentation of unrepresentative data, any references to a “random” selection of results to be presented in this work involve sorting the data in some logical way, performing a seed 0 shuffle, then selecting the shuffled elements in order. In this case, sorted by TIC ID then shuffled with seed 0.

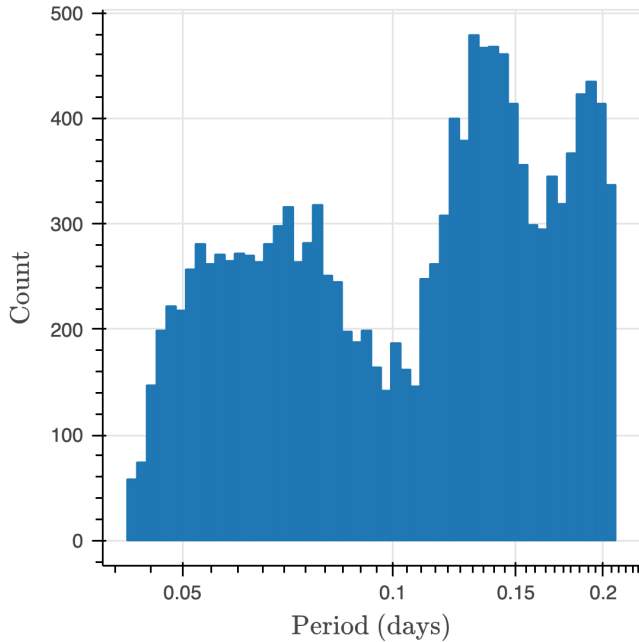


Figure 4. The period distribution of the variables as estimated by our pipeline. Note that for binary systems, this estimated period may be half of the system’s full orbital period.

the shorter period cluster corresponds to δ Sct. Throughout the rest of the results and analysis, we have assumed these two clusters to primarily contain MS binaries and δ Sct respectively. However, we emphasize that we have not performed any form of detailed modeling on these targets, and these two clusters almost certainly contain many targets which are not directly from these two classes of objects. The δ Sct cluster itself can be seen to be separated into two populations when comparing the period to the luminosity (Figure 6).

4.1. Partitioning the data

In the log luminosity vs log period relation, we have defined linear partitions to divide the three primary clusterings of data, splitting the data into a MS binary cluster, a primary ridge δ Sct cluster, and a second ridge δ Sct cluster (Figure 6). Several simple fitting metrics were originally used position these partitions. However, due to outliers, unknown detection efficiencies, and indistinct boundaries (notably between primary and second ridge δ Sct), these simple metrics produced imperfect partitions. Given that we have performed no detailed modeling of these different classes of objects and that these clusters certainly contain other types of objects, we opted to manually select these partitions rather than produce more convoluted fitting metrics. As such, we emphasize that these partitioned clusters should only be used for qualitative insights into the data and caution

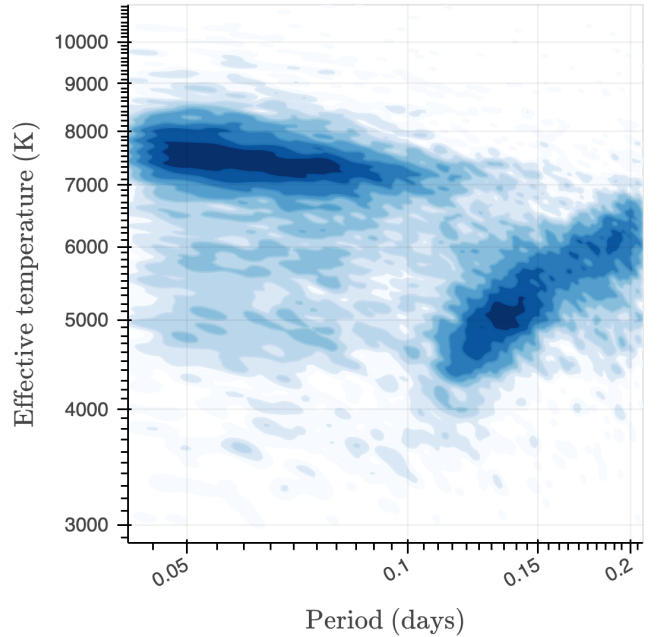


Figure 5. A kernel density estimation of temperature vs period of the variables. The effective temperature of the targets is taken from the TIC.

should be used when considering these clusters for any form of quantitative analysis. We also note that several smaller populations of interest likely exist in the data beyond these three, such as the small number of very high temperature variables discussed in Section 4.4.

Figure 6 shows luminosity vs period of the variables along with the selected partition lines. For a better qualitative comprehension of populations, we have partitioned the data into these three groups, and we color these clusters for many of the figures in this work. The MS binary cluster targets are shown in red, the primary ridge δ Sct cluster targets in blue, and the second ridge δ Sct cluster targets in yellow. These colors are consistent for any other figures using this clustering colorization, with the addition of gray for targets with unknown luminosity (which were then not included in the partitioning). This separation is more clear in the radius vs period relation (Figure 7), however, as the radius values are derived from the luminosity values along with some assumptions of the target, we use the luminosity vs the period relation to distinguish these clusters. Some caveats need to be considered when reviewing these results. First, the estimated period is the predominant period found during our search explained above. Notably, for binaries, this estimated period will typically be half the orbital period. Second, except for the estimated periods, the properties of the targets listed here are taken from the *TESS* catalog. Some of the *TESS* catalog values may be

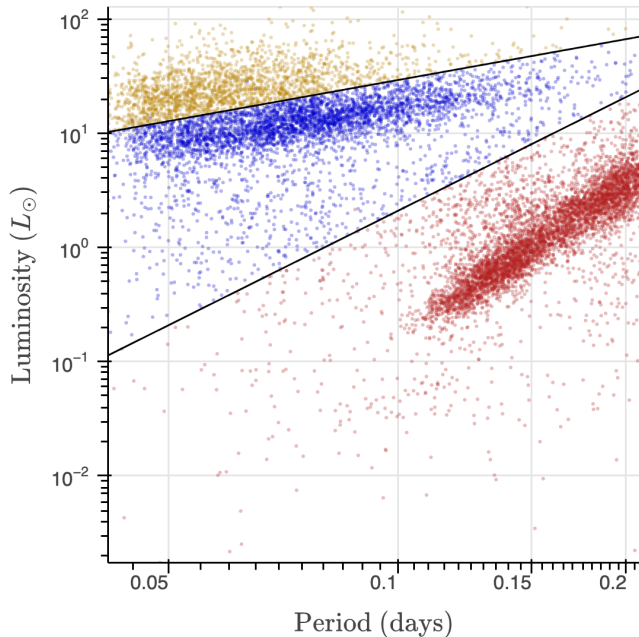


Figure 6. The luminosity vs the period of the variables. Note, these are the luminosities provided by the TIC which does not assume the targets are binaries. Cluster colors and partition lines are chosen based on a partitioning in log luminosity vs log period relations described in Section 4.1.

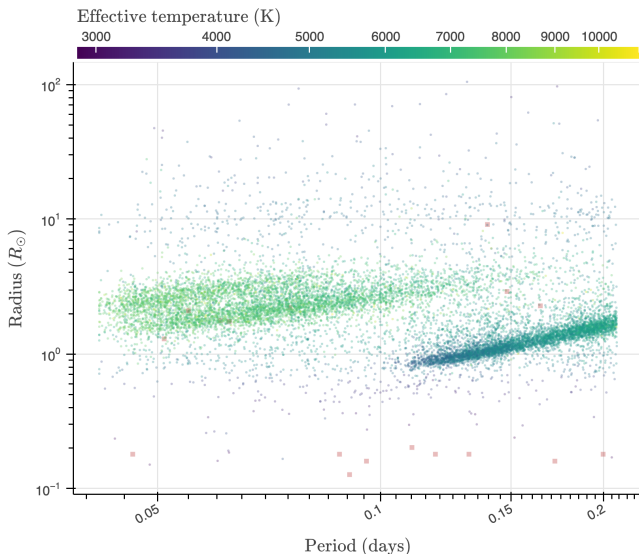


Figure 7. The radius vs the period of the variables color by the variable temperature. Due to high temperature outliers, the upper limit of the temperature scale is restricted to 11000K and any targets above this temperature are shown as red squares. Note, caveats given in Section 4.1 about how these values are estimated and how the estimate value may differ from the true value, especially in regard to binaries.

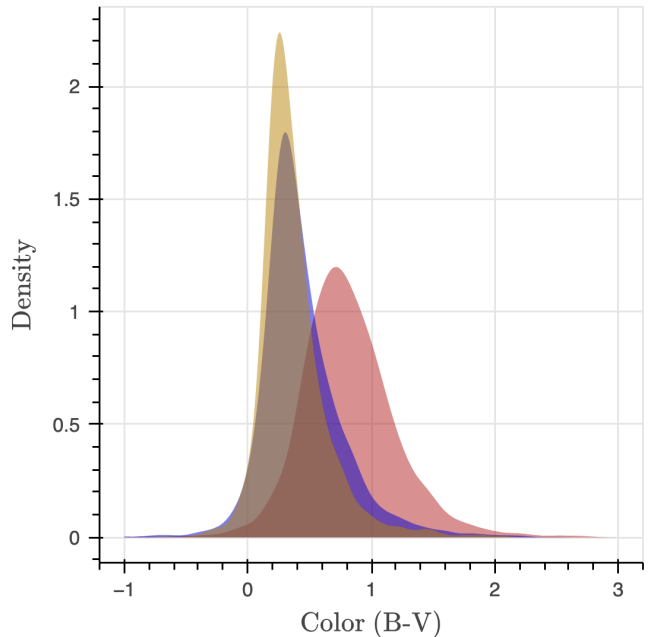


Figure 8. A kernel density estimation of the colors of the variables. Distributions are colored by the partitions described in Section 4.1.

taken from other existing catalogs or directly estimated through *TESS* observations. However, when these values are not either directly observed or known from existing catalogs, as is often the case, they may be derived values. Notably, luminosity, temperature, radii, and mass are derived from magnitude, color, and parallax. The details of how these values are derived can be found in [Stassun et al. \(2018\)](#). These derived values may cause some issues in the visualizations shown here. Most notably, these derived values are estimated for a single star, where in the case of binary systems this will result in a scale factor misrepresentation for various properties (e.g., radius).

As more detailed modeling of each of these targets with certainty is beyond the scope of this work, and we cannot know which of the targets do not actually belong in their assigned clusters, we present the original derived values. In any case where one of the properties of the target being plotted in a figure is unknown, that target will be excluded from the figure.

After partitioning the data as described above, we then visualize the distributions of the raw observed values for each partitioned cluster of data. The observed distributions of the photometric color of each cluster is shown in Figure 8. Similarly, Figure 9 shows the distributions of the *TESS* magnitudes of the clusters and Figure 10 the distributions of the parallax.

4.2. Binaries analysis

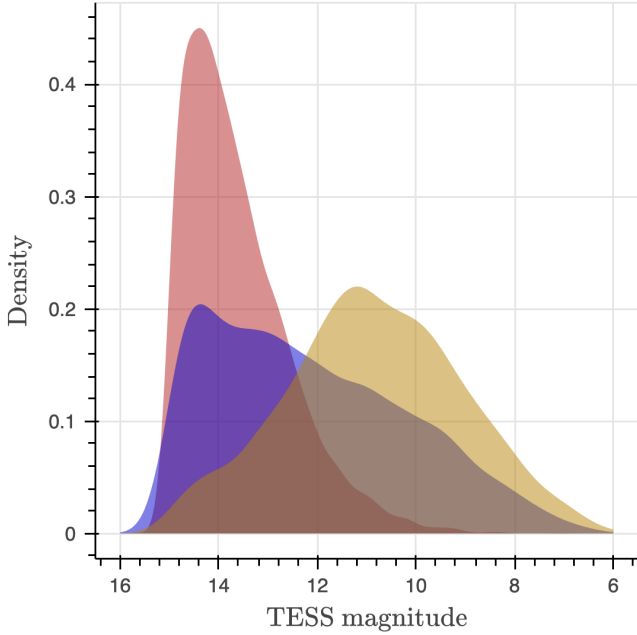


Figure 9. A kernel density estimation of the TESS magnitudes of the variables. Distributions are colored by the partitions described in Section 4.1.

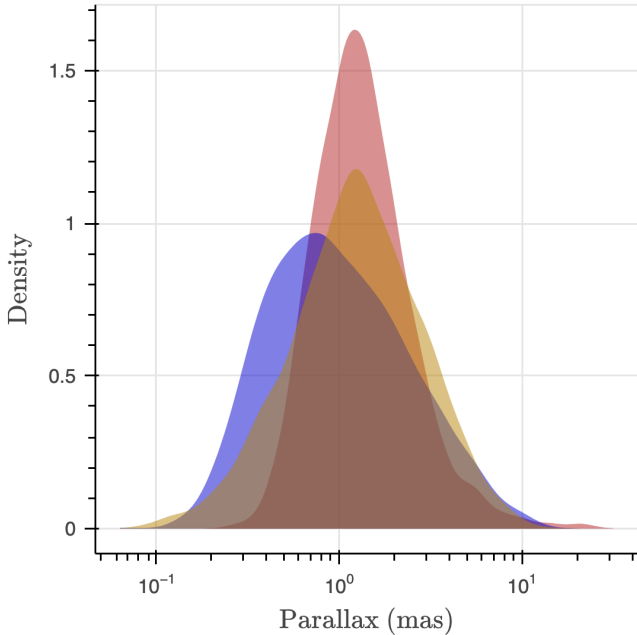


Figure 10. A kernel density estimation of the parallaxes of the variables. Distributions are colored by the partitions described in Section 4.1.

The short-period MS binary cluster contains 5574 targets, from which the overwhelming majority come from the population of binaries seen as the large grouping with longer periods in Figure 6. At the shorter period end of this population, there is a sharp cutoff at ~ 0.12 days.

With binaries, the full orbital period is twice this value at ~ 0.24 days. This is consistent with a known sharp cut-off of the period distribution of red dwarf binaries at ~ 0.22 days (Rucinski 1992; Norton et al. 2011). This cut-off is also seen in Figure 7 which shows radius vs period. As expected, this lower period is only found with cooler, smaller binaries, as the hotter binaries are larger and cannot easily orbit as closely.

This can easily be understood from basic stellar structure scaling relationships. For F, G, K stars with $0.5 \lesssim (M/M_\odot) \lesssim 2$, the radius scales roughly like $R = R_\odot (M/M_\odot)^{3/4}$. For an equal-mass binary $M_1 = M_2$, Roche lobe overflow will occur when the binary separation is roughly $a \approx 2.6R$, corresponding to a minimum orbital period of

$$\begin{aligned} T_{\text{orb}} &= 2\pi \sqrt{\frac{a^3}{G(M_1 + M_2)}} \\ &= 2\pi \sqrt{8.8 \frac{R_\odot^3}{GM_\odot} \left(\frac{M_1}{M_\odot}\right)^{5/4}} \\ &= 0.34 \left(\frac{M_1}{M_\odot}\right)^{5/8} \text{ d.} \end{aligned} \quad (1)$$

For a red dwarf binary with $M_1 = M_2 = 0.5M_\odot$, this corresponds to a binary period of 0.22d, just as we find empirically. Furthermore, if we use the mass-luminosity scaling for main sequence stars $L \approx L_\odot (M/M_\odot)^3$, we are able to recover the relationship $L \sim T_{\text{orb}}^{4.8}$, consistent with what we see in the lower track of Figure 6.

We folded the LCs on a period $p_{\text{fold}} = 2p_{\text{estimated}}$, where $p_{\text{estimated}}$ is the period estimated by our post-processing described in Section 3.4. Then, on these folded LCs, we applied a fast-Fourier transform, resulting in a fundamental mode with period p_{fold} and the first overtone mode with period $p_{\text{estimated}}$. Figure 11 shows the powers of the fundamental mode and the first overtone mode. Notably, we expect an increased fundamental for the binaries, as the differences between the two stars will primarily affect this mode.

In Figure 12, we see the relative amplitude of the periodic signal of the variables, again split into two primary populations. The top right population to be the binary population, with amplitudes that mostly range from ~ 0.02 to ~ 0.3 . These estimates only apply to targets with a known contamination ratio from *TESS*. As also evident in Figure 11, the binary cluster targets have, on average, a much larger relative amplitude than the δ Sct cluster targets.

4.3. Delta Scuti analysis

Similar to Figure 7, Figure 13 shows the targets in radius vs period space. Figure 7 is useful for seeing the

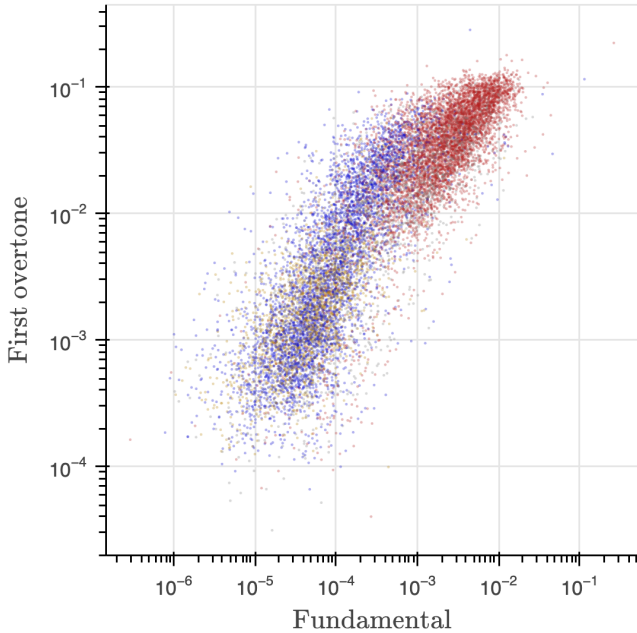


Figure 11. The powers of the fundamental and first overtone. Data points are colored by the partitions described in Section 4.1.

gap between the two δ Sct populations, while Figure 13 shows the cluster coloring after the partitioning has been made.

Figure 14 shows the temperature vs luminosity of the variables. Notably, the δ Sct targets are higher along the main sequence branch than the short-period MS binaries, which is expected, and the partitioning chosen divides δ Sct from the MS binaries fairly neatly.

Other works, including Ziaali et al. (2019); Barac et al. (2022), have shown a gap between the two δ Sct populations in log period space with a notable sparse region between the two populations, where the second ridge of δ Sct stars is known to have period of 0.5 that of primary ridge (Ziaali et al. 2019; Barac et al. 2022). This is usually shown with via the distribution of the distances in log period space to the partition line between the two populations, or an equivalent metric. The gap between the two ridges is not as clearly defined in our results as in Ziaali et al. (2019); Barac et al. (2022), with our distribution resulting in a short plateau in the distribution rather than a sparse region. However, we note that we have not performed a fitting to maximize this gap. Due to non- δ Sct targets certainly being within the presented clusterings and the uncertain detection efficiency of the neural network on each of the clusters, we don't expect such a fitting to be produce an accurate representation of the two δ Sct populations. See Section 4.1 for more details.

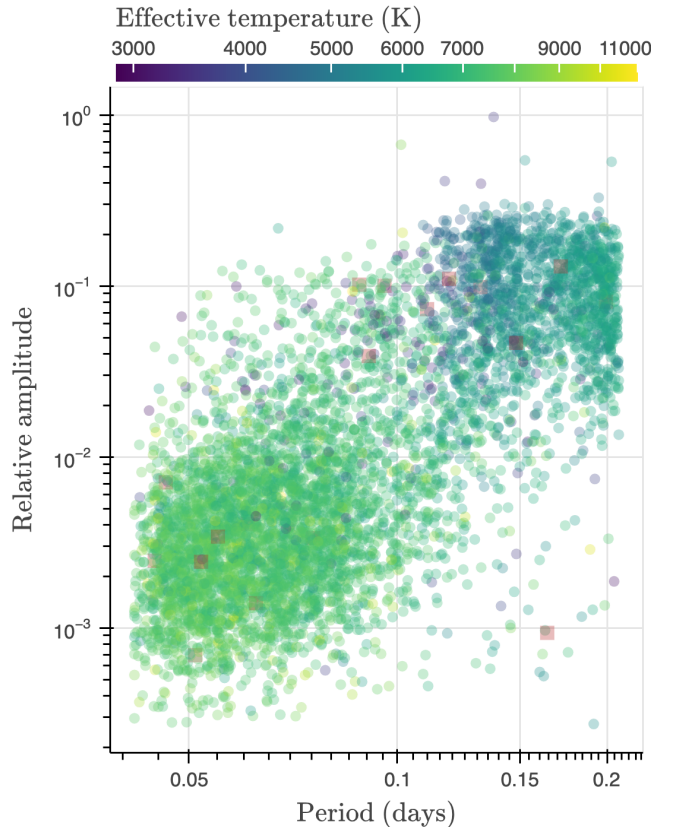


Figure 12. The relative amplitude vs the period of the variables color by the variable temperature. Due to high temperature outliers, the upper limit of the temperature scale is restricted to 11000K and any targets above this temperature are shown as red squares.

4.4. Hot targets analysis

Our NN detected nine hot periodic objects with effective temperatures ranging from 28,000 to 38,000 Kelvins. These appear to be blue subdwarf (sdB) stars, which are extreme horizontal branch stars with very high surface gravity and temperature (Baran et al. 2021, 2023; Schaffenroth et al. 2022).

There are three channels to formation of sdB stars involving close binary stellar pairs: common envelope, Roche lobe overflow (RLOF), and white dwarf (WD) mergers (Han et al. 2002). The common envelope channel produces short-period WD+sdB or sdB+MS binaries with periods ranging from 0.1 to 10 days. TIC IDs 333419799, 270491267, 396004353, 193092806, and 458785169 fall into this broad range. While the RLOF channel produces stars with periods exceeding 400 days and are thus not addressed by this work, the WD merger channel may produce single sdB stars that exhibit asteroseismic vibrational modes with periods of less than 0.1 days. Four hot periodic objects detected by our ML pipeline fall into this last category: TIC IDs 173295499,

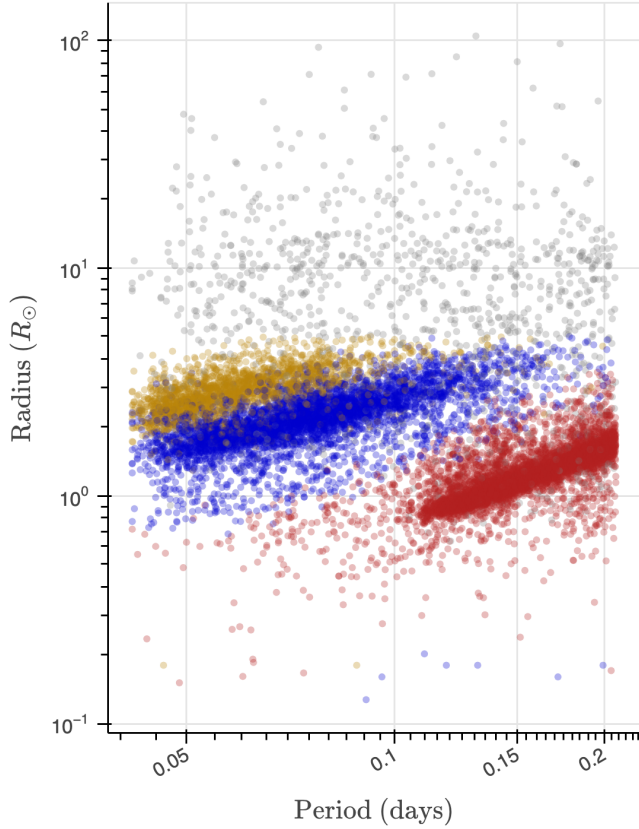


Figure 13. The radius vs the period of the variables. Data points are colored by the partitions described in Section 4.1.

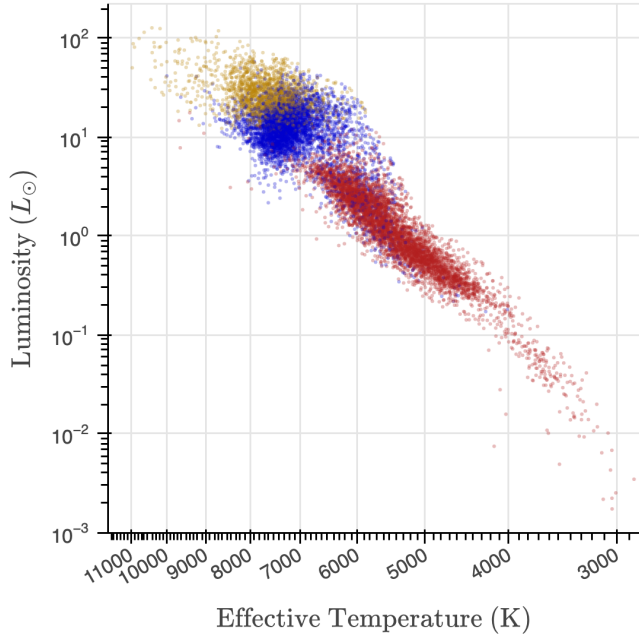


Figure 14. The effective temperature vs luminosity of the variables. Distributions are colored by the partitions described in Section 4.1.

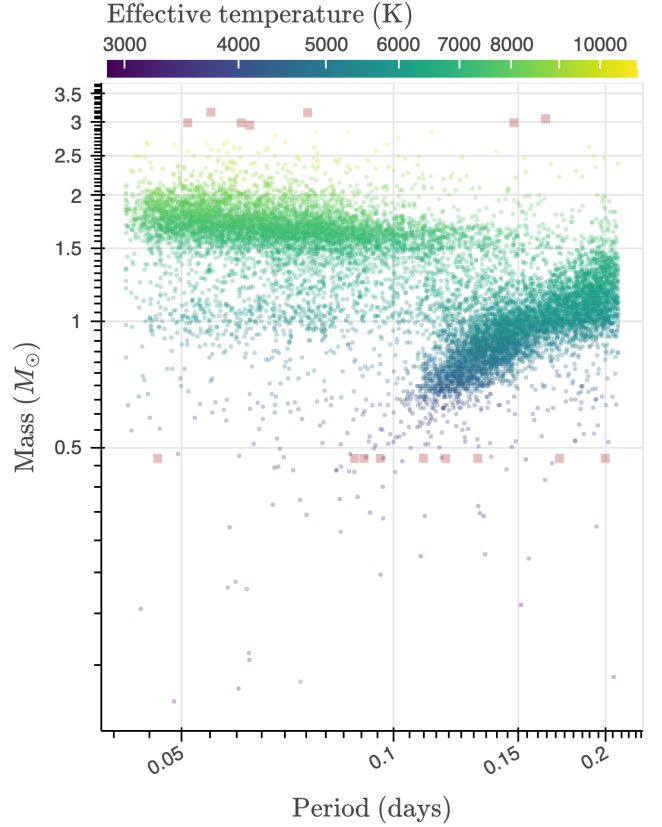


Figure 15. The mass vs the period of the variables. Due to high temperature outliers, the upper limit of the temperature scale is restricted to 11000K and any targets above this temperature are shown as red squares.

409644971, 99641129, and 367779738, with all but the final one having periods less than but very near 0.1 days. To be the best of our knowledge, TIC ID 367779738 has not previously been identified as a subdwarf in a close binary, but the remainder of these targets have previously been identified as subdwarfs in close binaries (Baran et al. 2021, 2023; Schaffenroth et al. 2022). All of these targets are identified spectroscopically as hot subdwarf stars by the Large Sky Area Multi-Object Fibre Spectroscopic Telescope data release 8 (Lei et al. 2023).

4.5. Miscellaneous analysis

Figure 15 shows the mass vs period of the variables. There is a sizable population of targets below the major δ Sct population. From our three clusters, most of this population comes from the δ Sct primary ridge cluster. However, this population may be a separate category of objects, or may simply be a group of targets whose mass is poorly estimated by the approach used by the TIC.

5. CONCLUSION

In this work, we presented a NN pipeline to identify short-period variable targets in *TESS* FFI data. This NN pipeline performs inference on a *TESS* 30-minute cadence light curve in ~ 5 ms on a single GPU. We also presented a collection of 14156 short-period variables, and provided a cursory analysis of the various populations of these targets. Within these populations, we examine two prominent populations consisting primarily of short-period MS binaries and the δ Sct stars. 5574 targets were identified in the MS binary cluster and 6188 were identified in the δ Sct clusters. Though not all, we expect the overwhelming majority of targets in each cluster to be of the class that is used to name each cluster. We provide this collection of targets in a supplemental file for more detailed analysis by specialists in the field for each of the populations.

For future work, our open-source NN framework allows for this work to be relatively easily extended. Notably, this work uses the *TESS* primary mission FFI data which had a 30-minute cadence. Later *TESS* FFI data has a higher cadence, which would enable searches for shorter period targets and more accurate post-processing. A simple change to the NN (*e.g.*, adjusting the stride lengths) would prepare it for training on this shorter cadence dataset. This, combined with the relatively fast inference speed of our network (~ 5 ms per LC on a single GPU), allows our method to be quickly deployed on new datasets.

6. ACKNOWLEDGMENTS

This paper includes data collected by the *TESS* mission, which are publicly available from the Mikulski Archive for Space Telescopes (MAST). Funding for the *TESS* mission is provided by NASA's Science Mission directorate.

Resources supporting this work were provided by the NASA High-End Computing (HEC) Program through the NASA Center for Climate Simulation (NCCS) at Goddard Space Flight Center.

This work has made use of data from the European Space Agency (ESA) mission *Gaia* (<https://www.cosmos.esa.int/gaia>), processed by the *Gaia* Data Processing and Analysis Consortium (DPAC, <https://www.cosmos.esa.int/web/gaia/dpac/consortium>).

The material is based upon work supported by NASA under award number 80GSFC21M0002.

Facilities: *Gaia*, MAST, NCCS, *TESS*

Software: *Astropy* (Astropy Collaboration et al. 2013, 2018), *Bokeh* (Bokeh Development Team 2020), *Eleanor* (Feinstein et al. 2019), *Keras* (Chollet et al. 2015), *Lightkurve* (Lightkurve Collaboration et al. 2018), *Matplotlib* (Hunter 2007), *NumPy* (Harris et al. 2020), *Pandas* (McKinney 2010), *pytest* (Krekel et al. 2004), *Python* (Python Core Team 2020), *Tensorflow* (Abadi et al. 2015)

REFERENCES

- Abadi, M., Agarwal, A., Barham, P., et al. 2015, TensorFlow: Large-Scale Machine Learning on Heterogeneous Systems. <https://www.tensorflow.org/>
- Astropy Collaboration, Robitaille, T. P., Tollerud, E. J., et al. 2013, *A&A*, 558, A33, doi: [10.1051/0004-6361/201322068](https://doi.org/10.1051/0004-6361/201322068)
- Astropy Collaboration, Price-Whelan, A. M., Sipőcz, B. M., et al. 2018, *AJ*, 156, 123, doi: [10.3847/1538-3881/aabc4f](https://doi.org/10.3847/1538-3881/aabc4f)
- Baade, W. 1944, *ApJ*, 100, 137, doi: [10.1086/144650](https://doi.org/10.1086/144650)
- Barac, N., Bedding, T. R., Murphy, S. J., & Hey, D. R. 2022, *Monthly Notices of the Royal Astronomical Society*, 516, 2080
- Baran, A. S., Sahoo, S. K., Sanjayan, S., & Ostrowski, J. 2021, *MNRAS*, 503, 3828, doi: [10.1093/mnras/stab668](https://doi.org/10.1093/mnras/stab668)
- Baran, A. S., Van Grootel, V., Østensen, R. H., et al. 2023, *A&A*, 669, A48, doi: [10.1051/0004-6361/202244888](https://doi.org/10.1051/0004-6361/202244888)
- Bedding, T. R., Murphy, S. J., Hey, D. R., et al. 2020, *Nature*, 581, 147
- Bokeh Development Team. 2020, Bokeh: Python library for interactive visualization. <https://bokeh.org/>
- Brasseur, C., Phillip, C., Fleming, S. W., Mullally, S., & White, R. L. 2019, *Astrophysics Source Code Library*, ascl
- Breger, M. 1972, *The Astrophysical Journal*, 171, 539
- Breger, M. 2000, in *Delta Scuti and Related Stars*, Vol. 210, 3
- Brown, A., Vallenari, A., Prusti, T., et al. 2018, *Astronomy & astrophysics*, 616, A1
- Burke, C. J., Levine, A., Fausnaugh, M., et al. 2020, ascl
- Chollet, F., et al. 2015, *Keras*, <https://keras.io>
- Cybenko, G. 1989, *Mathematics of control, signals and systems*, 2, 303
- Dong, C., Loy, C. C., He, K., & Tang, X. 2014, in *European Conference on Computer Vision*, Springer, 184–199
- Dupret, M.-A., Grigahcène, A., Garrido, R., Gabriel, M., & Scufflaire, R. 2004, *Astronomy & Astrophysics*, 414, L17
- Eastman, J., Siverd, R., & Gaudi, B. S. 2010, *Publications of the Astronomical Society of the Pacific*, 122, 935

- Feinstein, A. D., Montet, B. T., Foreman-Mackey, D., et al. 2019, *Publications of the Astronomical Society of the Pacific*, 131, 094502
- Graham, M. J., Kulkarni, S. R., Bellm, E. C., et al. 2019, *PASP*, 131, 078001, doi: [10.1088/1538-3873/ab006c](https://doi.org/10.1088/1538-3873/ab006c)
- Han, Z., Podsiadlowski, P., Maxted, P. F. L., Marsh, T. R., & Ivanova, N. 2002, *Monthly Notices of the Royal Astronomical Society*, 336, 449, doi: [10.1046/j.1365-8711.2002.05752.x](https://doi.org/10.1046/j.1365-8711.2002.05752.x)
- Handler, G. 2009, in *AIP Conference Proceedings*, Vol. 1170, American Institute of Physics, 403–409
- Harris, C. R., Millman, K. J., van der Walt, S. J., et al. 2020, *Nature*, 585, 357, doi: [10.1038/s41586-020-2649-2](https://doi.org/10.1038/s41586-020-2649-2)
- Hinton, G., Deng, L., Yu, D., et al. 2012, *IEEE Signal Processing Magazine*, 29, 82
- Hunter, J. D. 2007, *Computing in science & engineering*, 9, 90
- Jenkins, J. M., Twicken, J. D., McCauliff, S., et al. 2016, in *Software and Cyberinfrastructure for Astronomy IV*, Vol. 9913, International Society for Optics and Photonics, 99133E
- Jiang, D., Han, Z., Ge, H., Yang, L., & Li, L. 2012, *Monthly Notices of the Royal Astronomical Society*, 421, 2769
- Kahraman Alıçavuş, F., Çoban, Ç. G., Çelik, E., et al. 2023, *Monthly Notices of the Royal Astronomical Society*, 524, 619
- Krekel, H., Oliveira, B., Pfannschmidt, R., et al. 2004, *pytest x.y.* <https://github.com/pytest-dev/pytest>
- Krizhevsky, A., Sutskever, I., & Hinton, G. E. 2012, in *Advances in neural information processing systems*, 1097–1105
- LeCun, Y., Bengio, Y., & Hinton, G. 2015, *nature*, 521, 436
- Lei, Z., He, R., Németh, P., et al. 2023, *ApJ*, 942, 109, doi: [10.3847/1538-4357/aca542](https://doi.org/10.3847/1538-4357/aca542)
- Leshno, M., Lin, V. Y., Pinkus, A., & Schocken, S. 1993, *Neural networks*, 6, 861
- Lightkurve Collaboration, Cardoso, J. V. d. M., Hedges, C., et al. 2018, *Lightkurve: Kepler and TESS time series analysis in Python*, *Astrophysics Source Code Library*. <http://ascl.net/1812.013>
- Mateo, M., Hurley-Keller, D., & Nemec, J. 1998, *The Astronomical Journal*, 115, 1856
- McKinney, W. 2010, in *Proceedings of the 9th Python in Science Conference*, ed. S. van der Walt & J. Millman, 51 – 56
- Mikulski Archive for Space Telescopes. 2020, Mikulski Archive for Space Telescopes, <https://archive.stsci.edu/missions-and-data/tess>
- Norton, A. J., Payne, S., Evans, T., et al. 2011, *Astronomy & Astrophysics*, 528, A90
- Olmschenk, G., Silva, S. I., Rau, G., et al. 2021, *The Astronomical Journal*, 161, 273, doi: [10.3847/1538-3881/abf4c6](https://doi.org/10.3847/1538-3881/abf4c6)
- Powell, B. P., Kruse, E., Montet, B. T., et al. 2022, *Research Notes of the American Astronomical Society*, 6, 111, doi: [10.3847/2515-5172/ac74c4](https://doi.org/10.3847/2515-5172/ac74c4)
- Python Core Team. 2020, *Python: A dynamic, open source programming language*, Python Software Foundation. <https://www.python.org/>
- Ricker, G. R., Winn, J. N., Vanderspek, R., et al. 2014, *Journal of Astronomical Telescopes, Instruments, and Systems*, 1, 014003
- Rucinski, S. 1992, *Astronomical Journal (ISSN 0004-6256)*, vol. 103, March 1992, p. 960-966., 103, 960
- Rucinski, S. M. 2007, *Monthly Notices of the Royal Astronomical Society*, 382, 393
- Rumelhart, D. E., Hinton, G. E., & Williams, R. J. 1986, *nature*, 323, 533
- Schaffneroth, V., Pelisoli, I., Barlow, B., Geier, S., & Kupfer, T. 2022, *Astronomy & Astrophysics*, 666, A182
- Soszyński, I., Udalski, A., Szymański, M. K., et al. 2015, *Mem. Soc. Astron. Italiana*, 86, 257
- Stassun, K. G., Oelkers, R. J., Pepper, J., et al. 2018, *The Astronomical Journal*, 156, 102
- Stepien, K. 2007, arXiv preprint astro-ph/0701529
- Tenenbaum, P., & Jenkins, J. M. 2018, *TESS Science Data Products Description Document*, Tech. rep., EXP-TESS-ARC-ICD-0014 Rev D [https://archive.stsci.edu/missions/tess/doc ...](https://archive.stsci.edu/missions/tess/doc...)
- Xu, L., Ren, J. S., Liu, C., & Jia, J. 2014, in *Advances in Neural Information Processing Systems*, 1790–1798
- Zhou, D.-X. 2020, *Applied and computational harmonic analysis*, 48, 787
- Ziaali, E., Bedding, T. R., Murphy, S. J., Van Reeth, T., & Hey, D. R. 2019, *Monthly Notices of the Royal Astronomical Society*, 486, 4348

Table 1. A random sample of the short-period variables table. Due to page space constraints, some columns are excluded here which are include in the supplemental file. For the clusters, 0 corresponds to the δ Sct primary cluster, 1 corresponds to the δ Sct secondary cluster, and 2 corresponds to the δ Sct secondary cluster.

TIC ID	Period (days)	TESS magnitude	Color (B-V)	Parallax (mas)	Luminosity (L_{\odot})	Effective temperature (K)	Radius (R_{\odot})	Mass (M_{\odot})	Relative amplitude (contamination corrected)	Cluster
27399756	0.191597	14.3084	0.432	0.422676	5.294211	6206	1.99035	1.190	N/A	0
57104837	0.118362	12.5353	0.944	3.488980	0.400631	4688	0.95951	0.748	0.010296	0
63395663	0.048016	7.7804	-0.026	4.348280	29.135298	7904	2.87852	1.892	0.004903	2
84079248	0.133662	14.3848	0.961	1.592000	0.480714	4844	0.98444	0.790	N/A	0
85397534	0.041669	13.3796	0.192	0.428423	15.829482	7818	2.16868	1.860	N/A	2
129011402	0.059596	10.0443	0.167	2.768110	8.587992	7409	1.77860	1.690	0.001290	1
150395859	0.129224	14.2772	1.170	1.349820	0.515524	4987	0.96169	0.830	N/A	0
154089766	0.159397	13.4165	0.473	1.296250	1.262050	5747	1.13321	1.030	N/A	0
158321712	0.136393	9.1802	0.332	2.426560	21.206305	6954	3.17292	1.520	0.015252	1
164143903	0.178556	10.5526	0.444	2.956590	3.768160	6012	1.78928	1.111	0.074664	0
198457457	0.201747	9.4010	0.493	4.559980	4.690508	6565	1.67415	1.362	0.092000	0
202129305	0.066931	13.8895	0.657	0.414300	10.894480	6711	2.44164	1.430	N/A	1
229968259	0.065755	11.5932	0.325	1.334230	8.131012	7262	1.80141	1.640	0.012970	1
240936297	0.055294	7.6339	0.169	7.534510	11.373159	8086	1.71841	1.964	0.000989	1
250190926	0.185086	13.5371	0.407	0.538793	7.349079	6502	2.13631	1.330	N/A	0
259895398	0.085386	14.7899	0.530	N/A	N/A	4958	N/A	N/A	N/A	N/A
279161696	0.145065	11.6053	0.641	3.533400	0.948343	5318	1.14720	0.920	0.050170	0
287458386	0.055065	14.2555	0.451	0.482627	6.471795	7297	1.59176	1.650	N/A	1
289563235	0.053302	11.9361	0.792	1.351010	8.911157	7029	2.01295	1.550	0.002363	1
302280281	0.155104	13.9746	0.461	1.036030	1.320639	5741	1.16163	1.030	N/A	0
306738858	0.063785	9.6572	0.299	2.973500	12.022373	7781	1.90799	1.840	0.001603	1
329248237	0.127547	14.6418	0.467	1.352740	0.380904	4828	0.88212	0.780	N/A	0
330331931	0.076383	12.7128	0.706	0.977406	7.808430	6416	2.26155	1.290	0.059482	1
348363727	0.131109	14.7367	1.345	0.012004	N/A	4587	9.88582	N/A	N/A	N/A
367419535	0.200030	13.3578	1.152	0.256559	N/A	4646	8.94662	N/A	N/A	N/A
368313899	0.109381	13.7293	0.552	0.816118	4.217922	6033	1.87990	1.120	N/A	1
394171494	0.084973	13.3296	-0.650	2.136530	0.509137	5334	0.83553	0.920	N/A	0
453184196	0.163674	13.5680	1.017	0.406524	19.539179	6037	4.04076	1.120	N/A	1
453285891	0.147838	12.2257	0.716	3.463850	0.699419	4955	1.13484	0.820	0.124630	0
468663462	0.193995	14.4012	0.742	N/A	N/A	5109	N/A	N/A	N/A	N/A